Bollettino di Geofisica Teorica ed Applicata Vol. 60, n. 3, pp. 489-516; September 2019
DOI 10.4430/bgta0275

Lunar subsurface temperature profile modelling based on CE-1 and CE-2

W. Zhang

Department of Math&Physics, Shaoxing University, China and Department of AOP Physics, University of Oxford, U.K.

(Received: 28 December 2018; accepted: 18 March 2019)

ABSTRACT The subsurface temperature distribution of airless bodies across the Solar System can provide important clues to their formation and evolution. This paper investigates the lunar soil temperature profile using data from the recent Chinese lunar orbiting spacecrafts Chang'E 1 (CE-1) and Chang'E 2 (CE-2), to explore variations in the subsurface temperature of the Moon. These variations include heat flow information of the subsurface and the interior of the Moon. Before the launch of CE-1, the temperatures of deep layers of the Moon have only been measured at the landing sites of Apollo 15 and 17 by *in-situ* temperature probes. The CE-1 and CE-2 lunar orbiters were both equipped with a 4-frequency microwave radiometer (MRM) to detect the lunar surface brightness temperature (TB) and to retrieve data on lunar regolith thickness, temperature, dielectric constant, and other related properties. The MRM can penetrate to a nominal depth of 5 m in the subsurface with the 3 GHz channel. This research aims to develop a radiative transfer forward model for an airless body and then utilise MRM data to study an observed anomaly of 2 m deep TBs measurements in the Oceanus Procellarum region on the lunar subsurface. After initial validation of the MRM data and modelling of the lunar regolith parameters, a multi-layer radiative transfer forward model has been derived using the fluctuation dissipation theorem. The forward model calculates the radiometric contribution from several depths to the TB that would be observed by the MRM instrument around the Moon (at different frequencies), as a basis for an inverse method. Sensitivity analysis indicates that, as expected, mineralogy and density information are very important to the inverse calculation. The FeO/TiO2 distributions were also used to derive the bulk density of the lunar surface which was also incorporated into the calculation. The forward model was, then, used to invert the MRM measured TB data to generate 2-m depth subsurface temperature profiles. The provisional results show that, as expected, the 2-m subsurface temperature is potentially correlated to the distribution of radioactive elements such as uranium and thorium in the lunar crust. The 2-m subsurface temperature map was then converted to a lunar heat flow map, which was validated by the Apollo 15 and 17 measurements. Inspecting this heat flow map, abnormal high heat flow in the Oceanus Procellarum KREEP Terrain (PKT) region was noticed. The PKT is enriched with a high abundance of radioactive elements such as uranium and thorium. Hence, a heat flow model based on radioactive elements as well as internal cooling was built to investigate such a finding.

Key words: heat flow, KREEP region, MRM.

1. Introduction

The main problem addressed by this paper is to determine the appropriate technique to interpret the microwave data on an airless body, such as the Moon. To answer this question, this paper focuses on the establishment of a microwave-sounding model for airless bodies including the quantification of lunar subsurface parameters, the transmission analysis of microwave radiation in the lunar regolith and the retrieval.

1.1. Importance of studying lunar subsurface temperature and heat flow

Missions exploring the lunar surface have greatly improved our understanding of the Moon's composition, origin, and evolution. Over geologic time, the lunar surface has been shaped by impacts, solar irradiation, and cosmic rays. After the Apollo and Luna landings in the 1970s, subsequent lunar exploration mainly used visible and infrared remote sensing to study the topography, composition, and near-surface thermal properties of the Moon.

However, information about the properties of the lunar subsurface, deep structural features and thermal environment is hard to determine, except for measurements obtained at the Apollo and Luna landing sites and returned lunar samples (Heiken *et al*., 1991). Geochemical surveys of returned lunar samples cannot provide direct information on the global composition and physical properties of the subsurface. As a result, knowledge of the Moon's basic geophysical properties including its internal structure which can help in constraining theories about its formation and evolution, remains lacking, and our understanding of the lunar origin and evolution is still limited (Hartmann, 1986). Due to these limitations, the lunar subsurface, deep structural features and thermal environment are still not fully understood. For example, the Moon that once thought to be cold and dead, may have experienced recent volcanic eruptions in the last tens millions years (Braden *et al*., 2014) and hence some parts of the Moon may be warmer than previously thought (Braden *et al*., 2014).

The thermal evolution and current thermal state of the Moon is a very important active area of research. By measuring the internal heat flow and the deep subsurface temperature profile (1-5 m) of the Moon, this work can trace back and determine the lunar core's thermal flow. The results are important for developing theories about the Moon's crust and any residual activity in its core. Specifically:

a) modelling the heat flow of the Moon as part of diagnostic tests for thermal evolution models. Heterogeneities affect *in-situ* measurements of heat flow, so it is not possible to draw conclusions about the whole Moon without global coverage;
b) using the distribution of radioactive elements to constrain the evolution of the lunar crust and its connection to differentiation processes during the Moon's formation. This can help us understand the quantity and distribution of radioactive elements between the crust and mantle, part of its differentiation history. The heat flow of the Moon greatly depends on the concentration of a large number of radioactive isotopes, especially uranium, thorium and potassium. However, the distribution of these isotopes below the surface of the Moon remains unknown. Measurements by e.g. the Lunar Prospector spacecraft (Lawrence *et al*., 2002b), only observe the abundance and distribution of radioactive isotopes in the shallow surface (approximately 20 cm) of the Moon. Also, according to heat flow measurements made by the Apollo 15 and 17 missions, the concentration of uranium on

the Moon varies between an Earth-like 20/21 ppb (Warren and Rasmussen, 1987) and 46 ppb (Langseth *et al*., 1976);

c) to understand the nature of the Procellarum KREEP Terrane (PKT)[1]. Geochemical surveys have shown (Haskin, 1998) that KREEP mainly occurs in the north-western quadrant of the Moon (Fig. 1). The thermal modelling by Wieczorek and Phillips (2000) showed that the high radioactivity of PKT could contribute as much as 20 mW/m^2 of heat flow at the centre of PKT, so it is a significant energy source that needs to be quantified. By comparing the heat flow at the centre of the PKT with the average heat flow of the Moon, the overall abundance of radioactive materials can be estimated. The Apollo measurements were made at only two locations (Fig. 1b) so the available samples may not reasonably represent the concentration of radioactive elements in KREEP (Korotev, 1998);

d) understanding the lunar subsurface temperature distribution is also critical in studying the timing and evolution of lunar volcanism (Andrews-Hanna *et al*., 2014). The detection of any anomalous hotspots not correlated with KREEP terrain needs to be investigated.

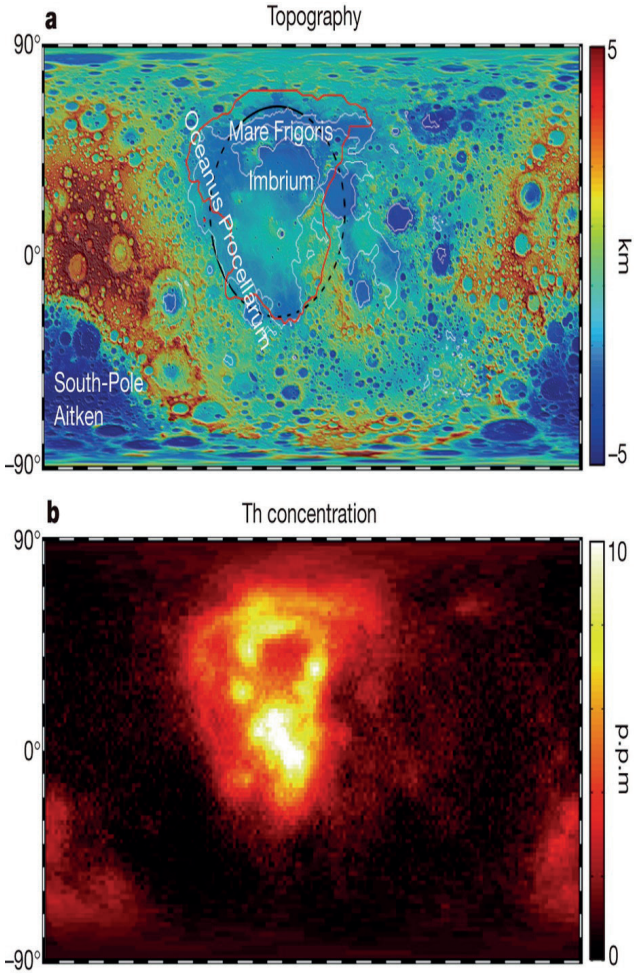

Fig. 1 - Global maps of the Moon showing: a) topography; b) Th concentration (Andrews-Hanna *et al*., 2014). The red line on the topographic map shows the extent of the PKT region. The PKT region is also clearly visible in the mapped Th concentration (Lawrence *et al*., 1998). The circular rim of the Oceanus Procellarum region is shown by a black dashed line in panel a (Whitaker, 1981). The outline of the Maria is also shown by white lines (Hiesinger *et al*., 2010).

[1] KREEP is an acronym built from the letters K (potassium), REE (rare Earth elements) and P (phosphorus).

1.2. The advantages of microwave remote sensing measurements for determining lunar heat flow

Global measurements of lunar heat flow are required for understanding the Moon. Subsurface heat flow can generally be estimated in two ways, *in-situ* measurements and by remote sensing. *In-situ* measurements involve drilling a hole in the lunar surface and determining the temperature at specific depths.

Measurements at the Apollo 15 and 17 sites are complicated to interpret because of experimental difficulties, including making sure the regolith was not compacted prior to inserting the heat probe (Heiken *et al*., 1991). In addition, both the Apollo 15 and 17 heat measurement sites were in Maria regions near the lunar equator (Fig. 1a) and thus cannot be easily compared with other areas. More importantly, the Apollo 15 and 17 sites are in, or nearby, KREEP rich terrain. Therefore, they cannot represent the lunar crust as whole (Hagermann and Tanaka, 2006).

The second way to measure temperature profiles is by remote sensing. Since September 2009, the Diviner Lunar Radiometer Experiment (Diviner) on the Lunar Reconnaissance Orbiter (LRO) (Paige *et al*., 2010) has been acquiring an extensive set of thermal emission measurements from the lunar surface at infrared wavelengths generating global bolometric maps of the top 2-mm surface temperatures. Remote sensing techniques such as Diviner, that use thermal infrared or visible wavelengths, can only provide compositional and temperature information to a depth of a few millimetres. As a result, data on the global, deep (50 cm or more) lunar subsurface temperature structure, mineralogy, and heat flow are limited.

Longer electromagnetic wavelengths in microwave region of the spectrum (>1 mm) have much greater penetration depths and so can potentially probe at greater depths than infrared techniques alone, thereby revealing the lunar regolith's deeper (>50 cm) temperature structure. In addition to regolith temperature, microwave remote sensing measurements can also potentially give information about other properties such as dielectric constant and density, etc.

Microwave remote sensing aims to look into the shape and structure of an object by detecting radiation reflected or emitted at wavelengths that are typically >1 mm. Microwave remote sensing techniques developed for Earth measurements in the late 20th century can also be applied to other planets and extraterrestrial bodies, including the Moon. Using these longer wavelengths, temperatures at depths of several metres can, then, be estimated. Therefore, microwave remote sounding can compensate for the shortcomings of other remote sensing techniques (which can only penetrate <2 cm), providing additional data. However, the modelling of microwave remote sensing is challenging because it depends on many parameters including mineralogy, density, heat capacity, and dielectric constant, etc.

Depending on the working principle, microwave remote sensing devices can be divided into two categories:

1. active, which proactively transmits microwave signals and then receives the reflected or scattered signal off of a target in a similar way to radar;
2. passive, which works in a similar way to an infrared radiometer such as Diviner by using a highly sensitive microwave receiver to obtain the faint radiation signals of the target.

Since the 1960s, passive microwave propagation from the surface of the Earth has been the subject of numerous studies. However, water absorption prevents measurements at appreciable

depths (~5 cm) (Tsang *et al*., 1975; Njokuand Kong, 1977; Burke *et al*., 1979). Therefore, microwave transmission on Earth does not typically contain information on soil thickness and underlying rocks, but can be used to measure soil humidity. Fortunately, this problem does not exist in the desiccated environment of the Moon.

Furthermore, recent Chinese remote sensing satellites have carried microwave radiometers, which can measure the deep subsurface. The original goal of these instruments was to map ^{3}He composition (Wang *et al*., 2008).

Both CE-1 and CE-2 lunar orbiters were equipped with a passive microwave radiometer (MRM) to measure the brightness temperature of the lunar surface (Li *et al*., 2010). The measured lunar brightness temperature (TB) can then be used to determine the lunar subsurface temperature after taking into account certain lunar regolith properties (e.g. density, heat capacity, mineralogy, dielectric constants, etc.). Data in the microwave region of the electromagnetic spectrum measured by instruments, such as the MRM on CE-1 and CE-2, can penetrate deeper (up to 5 m) into the lunar subsurface than visible or thermal infrared instruments (~2 mm). This opens a window into deep lunar subsurface temperature and heat flow, which presents a "microwave Moon."

1.3. Outline of this paper

The main problem addressed by this paper is to determine the appropriate technique to interpret the microwave data on an airless body, such as the Moon. To answer this question, this paper focuses on the establishment of a microwave-sounding model for airless bodies, with the Moon as an example, including the quantification of lunar subsurface parameters, the transmission analysis of microwave radiation in the lunar regolith, and the retrieval of subsurface temperature.

Temperature profiles at metre depth around the equator region can, then, be derived from the 1D thermal diffusion equation using the surface temperatures provided by Diviner's infrared observations as a boundary condition. Based on a microwave radiative transfer model and using the fluctuation dissipation theorem, the 2-m subsurface temperatures and heat flow of the Moon are inverted from the CE-1 and CE-2 multichannel microwave brightness temperatures.

To summarise the work flow of this paper, the first step was extracting and plotting the brightness temperatures derived from the CE missions. Then the MRM data was validated in section 2 by comparing it to the Diviner data. After validating the MRM data, the parameters needed to develop an inversion model of the MRM data were investigated in section 3. These parameters included lunar regolith density, specific heat capacity, dielectric constant, and conductivity. The number of layers required in the inversion model were also investigated.

In section 3, a one dimensional thermal vertical model was developed and several thermal latitude models were discussed. The MRM data was further validated by comparing the measurements with the theoretical thermal depth simulations of the one dimensional thermal vertical model. The modelled temperature profile of the lunar regolith varied mainly within the top 20 cm. Below 20 cm the temperature was stable with depth (diurnal variation $<\pm 5$ K).

A microwave radiative transfer model for the CE-1 and CE-2 MRM data was developed in section 4, which was used as a forward model in the later inverse scheme. The forward model calculated the contribution of each depth to the TB (at different frequencies), thereby determining the depth that each MRM channel sounded to. The inverse temperature vertical

profile could, then, be compared with the Apollo 15 and 17 site measurements. The MRM measured temperature profile beneath the lunar surface matched well with the calculations provided by the theoretical model simulation and with the Apollo *in-situ* measurements. Section 4 also explored the error analysis by using both standard error propagation and Monte Carlo analysis. The main error sources were found to be Maria mineralogy and the density of the lower bedrock, whereas the TB error from the instrument or the highland mineralogy displayed a much smaller influence.

2. MRM details and validation

2.1. MRM instrument details

Both CE-1 and CE-2 MRMs (Table 1 and Fig. 2c) have been used to detect the TB of lunar surface and retrieve lunar regolith thickness, temperature, dielectric constant and other related properties (Wang *et al*., 2008). Details of the instrument and ground calibrations are described by Wang *et al*. (2010).

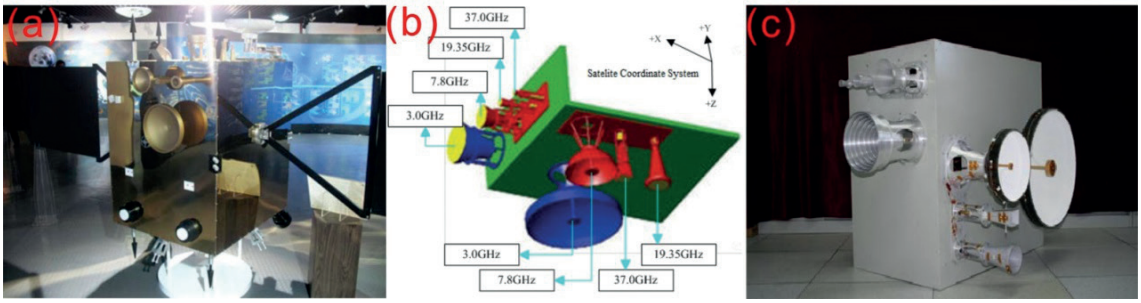

Fig. 2 - a) CE-1 spacecraft; b) CAD model of MRM on CE-1; c) MRM instrument. The size of CE-1 is 200×172×220 cm^3, and the size of the MRM instrument is 120×172×90 cm^3.

Each frequency channel has three input sources, namely the lunar observing antenna, the cold-air calibration antenna and the hot load antenna. The three antennas share one receiver, so the MRM works with two in-orbit calibrations. High and low temperature calibrations were used to determine the microwave radiometer calibration equation (Eq. 1). This calibration equation can be used to accurately calibrate the lunar regolith microwave TB captured by the observing antenna. In addition, the receiver is equipped with a temperature measurement circuit and can perform real-time temperature monitoring of the 28 key points in the antennae. The temperature variations in all operational orbits were between 12 and 23 K, with no more than 5 K temperature variation for each detected orbit period receiver (Wang *et al*., 2010). According to the following Eq. 1, the performance was, then, acceptable to meet the radiometric accuracy requirement of <0.5 K. Assuming a nominal lunar regolith mineral content of S=10% (S is defined as S=Ti%+Fe%), density of 1.9 g/cm^3, predicted penetrating depths are <0.5, <1.0, <2.0, ≥5.0 m at 37.0, 19.35, 7.8 and 3.0 GHz, respectively (Wang *et al*., 2008; Li *et al*., 2010).

Table 1 - Basic performance information of the MRMs (Wang *et al*., 2010).
Operation details:

Flight control period	Operating time (h)	Effective access time (h)	Coverage
2007.11.27~2008.01.27 (first flying period)	1380.7	1160.3	84.0%
2008.01.30~2008.02.04 (first side-flying period)	120.9	100.4	83.0%
2008.05.15~2008.07.29 (second flying period)	1624.6	1396.6	86.0%
2008.11.12~2009.01.14 (life Extension)	858.2	705.8	82.0%
Total	3984.4	3363.1	84.4%

Instrument details:

Name	CE index
Frequency (GHz)	3.0(±1%), 7.8(±1%), 19.35(±1%), 37.0(±1%)
Integral time (ms)	100(±15%), 200(±15%), 500(±15%), 500(±15%)
Temperature resolution (K)	≤0.5
Orbits number	2401
Orbit Height	100 km
Spatial resolution	17.5 km
Orbital inclination	31.0 degrees

2.2. Data acquisition and lunar surface coverage

The CE-1 spacecraft was placed into lunar polar orbit and ground track coverage was repeated twice a month, that was, during lunar day and night. The altitude of satellite orbit was approximately 200 km in the early stage of satellite operation. However, the height of the satellite orbit was reduced to approximately 100 km in the extended mission period, generating an additional 210 circular orbit tracks of data at higher spatial resolution (from 35.0 to 18.2

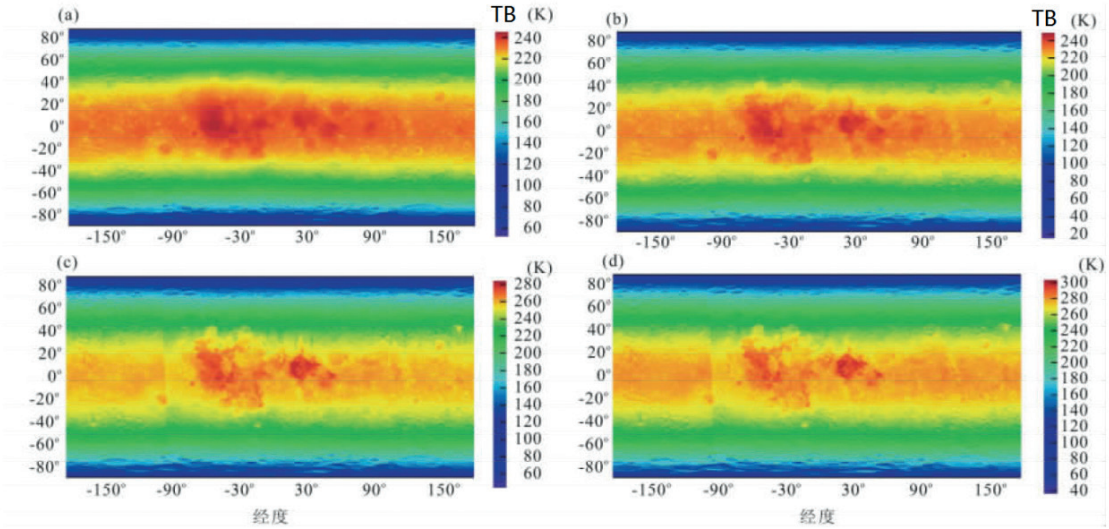

Fig. 3 - Interpolated maps of the TB distribution on the lunar surface obtained by CE-2 MRM during the lunar day (mid-day time): a) 3.0 GHz; b) 7.8 GHz; c) 19.35 GHz; and d) 37.0 GHz (Feng *et al*., 2013).

km). CE-2 was very similar to CE-1. The only difference of note was that CE-2 had a much smaller antenna footprint size (17.5 compared to 35.0 km) due to its 100 km orbital altitude. Interpolated maps of the TB distribution on the lunar surface obtained by one month of CE-2 MRM data during the lunar day are plotted in Fig. 3 (note: the plotted TB is not the real temperature of the lunar soil but the TB derived from the MRM data).

In Figs. 3c and 3d, an apparent discontinuity can be noticed at longitude -100°. Such a discontinuity is caused by the conjunction of the first and last tracks of data. Although the detection areas of the first and last tracks are similar, the solar elevation angles of the two tracks can be quite different, which result in significant differences in derived TB from the high frequency channels (panel c is 19.35 GHz TB, while panel d is 37.0 GHz TB). For low frequency channels such as 3 GHz channel, solar elevation angle is not as important due to the increased sounding depth.

2.3. Data validation

The 3 GHz channel of the MRM can sense temperature to depths of approximately 5 m below the lunar surface. Therefore, comparing data obtained from MRM with those gathered from other instruments, such as the Diviner radiometer (which can sense temperatures to depths of 2 mm) of the LRO, is of great interest (Paige *et al*., 2010).

The Diviner Lunar Radiometer Experiment is a multi-channel solar reflectance and infrared radiometer with 7 spectral channels, of which 3 spectral filters are near 8 μm wavelengths and four filters cover approximately 13-23, 25-41, 50-100 and 100-400 μm wavelengths (Paige *et al*., 2010). Data is collected in a push-broom configuration across the surface of the Moon. The radiometer charts the temperature of entire lunar surface at approximately 500 m horizontal scales. To identify potential ice deposits, Diviner has been mapping the global thermal state of the Moon since July 2009.

Overlaps between CE-1 and Diviner data at specific local times were checked to verify the validity of both the Diviner and CE-1 MRM data as an independent inter-comparison of both data sets. CE-1 data was checked against the Diviner results when sampled on a similar spatial grid (Fig. 4). The effects of topography and local time were minimised by extracting Diviner data with local times and latitude/longitude coordinates within the region with the most CE-1

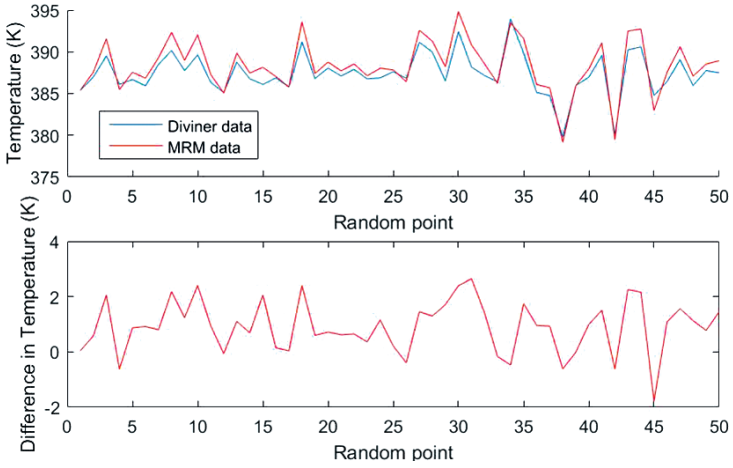

Fig. 4 - A comparison graph which takes 50 random equatorial latitude/longitude points and compares the maximum Diviner measured temperature to the MRM data (the 37 GHz channel). The Diviner and this MRM channel sense to almost the same depth.

flyby times, e.g. 0°-5° N and 40°-35° W for midday (11 a.m. - 1 p.m. local time) and 0°-5° N and 140°-145° E for midnight (11 p.m. - 1 a.m.). Data of two instruments were consistent, because their TBs matched within expected variation (±5 K) (Fig. 4).

3. Numerical model of lunar regolith and lunar soil: thermal environment simulations

Given that, to a first order at least, the MRM instruments are measuring the thermal-physical properties of the lunar regolith. It is important to define the controlling physical parameters such as density, permittivity, and specific heat capacity as well as the sources of input energy. By combining these sources of information it is then possible to start modelling the expected lunar sub-surface temperature structure using thermal transfer models appropriate for the analysis of microwave remote sensing data.

3.1. Bulk density

The depth profile of the lunar surface and subsurface can be divided into three parts (Heiken *et al*., 1991) (Fig. 5):

1. a 2-cm dust layer on the surface;
2. a 5- to 10-m soil layer just below the dust layer;
3. a thick lunar bedrock layer below the soil layer (Fa and and Wieczorek, 2009).

The top two parts of the lunar regolith are referred to as the upper lunar regolith.

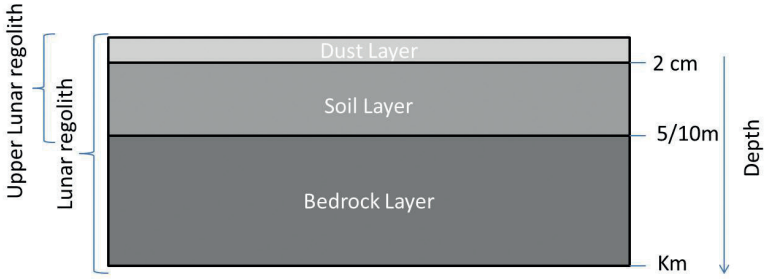

Fig. 5 - Depth profile of the lunar surface and subsurface.

Due to the lack of atmosphere and erosion processes on the lunar surface, individual grains that make up the upper lunar regolith layers have a 'pointy' structure. This combined with the low gravity of the Moon (1/6 that of Earth's) results in the upper lunar regolith layers being highly porous with large spaces between individual grains. The bulk densities of the upper lunar regolith layers are defined as the mass per unit volume of the lunar regolith including these spaces.

Vasavada *et al*. (1999) assumed that the bulk density of the top 2-cm lunar dust layer is 1.3 g/cm^3, and of lunar soil layer is 1.6-2.1 g/cm^3 (Heiken *et al*., 1991). The relationship of the lunar soil layer bulk density profile with depth can be described as follows (Heiken *et al*., 1991):

$$\rho = 1.92\frac{z+12.2}{z+18} \tag{1}$$

where z is the lunar regolith depth, in centimetres.

Measurements of the Apollo core samples show that the average density of the upper lunar regolith layer increases with depth (Cartier *et al*., 1973). Knowledge of the density profile allows the study of another important factor: the dielectric permittivity.

3.2. Dielectric permittivity

The dielectric permittivity constant is important for modelling the MRM data because it determines from what depth the received radiance was emitted (see Figs. 6 and 7). The results of measurements on lunar samples from the Apollo and Luna missions (Heiken *et al*., 1991) show that when the frequency is greater than 1 MHz, the real part of the permittivity (dielectric constant) of the lunar regolith is dependent on the density of the lunar regolith assuming a nominal chemical composition (Heiken *et al*., 1991). Hence the permittivity ε_r' can be estimated using an empirical relationship:

$$\varepsilon_r' = 1.919^{\rho} \tag{2}$$

The imaginary part ε_r'' of permittivity of the lunar soil is the product of the real part of the permittivity and the loss angle tangent[2] of lunar soil (Olhoeft and Strangway, 1975; Heiken *et al*., 1991):

$$\varepsilon_r'' = \varepsilon_r' \times \tan\delta \tag{3}$$

where $\tan\delta$ is the dielectric loss angle tangent of the lunar soil.

The current well-accepted theory (Olhoeft and Strangway, 1975) is that the loss tangent is not only a function of the density of the lunar soil, but also related to the TiO_2 and FeO abundance (expressed by S). This can be modelled using a 3D regression equation, which was derived from the lunar soil samples (Olhoeft and Strangway, 1975):

$$\tan\delta = 10^{0.038\cdot(\%TiO2+\%FeO)+0.312\rho-3.260} \tag{4}$$

where $\%TiO_2$ and %FeO are TiO_2 and FeO abundances in the lunar soil respectively.

We define S as sum of TiO_2 and FeO content present in minerals found in lunar soil.

3.3. Thermal conductivity

According to Heiken *et al*. (1991), the upper 2-cm layer of lunar regolith (dust layer) has an extremely low thermal conductivity (1.5×10^{-5} W/cm^2 measured at the Apollo 15 Landing Site). Below the dust layer the soil layer has a much larger thermal conductivity (7.5×10^{-5}~10.5×10^{-5} W/cm^2). This is because thermal conductivity is dependent on density and lunar dust layer has a much lower density of 1.3 g/cm^3 compared to the soil layer density of 2.1 g/cm^3. The variation with depth of thermal conductivity of lunar soil can be expressed as (Mitchell and de Pater, 1994):

[2] Dielectric loss angle tangent: dielectric loss measures a dielectric material's inherent dissipation of electromagnetic energy into heat, usually parameterised in loss angle tangent $\tan\delta$.

$$k = k_c[1 + \chi(\frac{T}{T_{350}})^3] \quad (5)$$

where k_c is the phonon conductivity, χ is the ratio of "radiative conductivity" to phonon conductivity at 350 K, T is subsurface temperature in Kelvin and T_{350} is 350 K. Vasavada *et al*. (1999) gave the coefficients of k_c and χ for lunar dust and soil layers as: k_c=9.22×10^{-4} Wm^{-1}K^{-1}, χ=1.48 for the dust layer, and k_c=9.3×10^{-3} Wm^{-1}K^{-1}, χ=0.073 for the soil layers. And this is in agreement with recent Hayne *et al*. (2017) work, which get k_c=7.4~10×10^{-4} Wm^{-1}K^{-1} at the surface.

3.4. Specific heat capacity

Horai and Fujii (1972) found that the specific heat (C) of the lunar regolith varies with temperature. Later Jones *et al*. (1975) provided an empirical third-degree polynomial formula (determined by the least-squares technique based upon Apollo 11 regolith sample data) that determined its dependence on temperature (70-400 K):

$$C(T) = c_1T^3 + c_2T^2 + c_3T + c_4 \quad (6)$$

where C is in units of J·g^{-1}K^{-1}. Urquhart and Jacksky (1997) found that c_1=5.19×10^{-9} J·g^{-1}K^{-4}, c_2=–8.20×10^{-6} J·g^{-1}K^{-3}, c_3=4.98×10^{-3} J·g^{-1}K^{-2}, c_4=–15.48×10^{-2} J·g^{-1}K^{-1}.

3.5. Vertical distribution of lunar subsurface temperature as the first estimate

3.5.1. Previous thermal diffusion modelling work

There is currently no conclusive data on the Moon's vertical temperature distribution. The sub-surface heat flow has been measured at only two landing sites (Apollo 15 and Apollo 17) and these results show that the temperature fluctuations due to the diurnal wave decrease with depth until at about ~0.8 m below the lunar surface where they become negligible (Horai and Fujii., 1972; Heiken *et al*., 1991).

1D thermal diffusion models, such as by Vasavada *et al*. (1999), predict the surface and subsurface profile of the lunar soil. The predicted surface and subsurface temperature structure can then be used in a microwave radiative transfer forward model to predict the TB observed by the MRM instrument (Fig. 6).

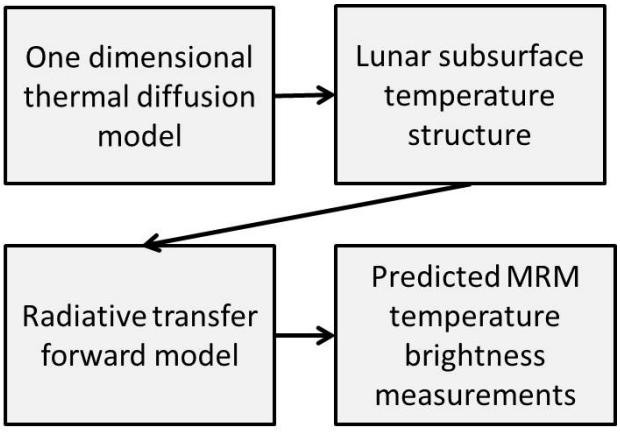

Fig. 6 - Model flow and clarification: a thermal diffusion model is used to describe subsurface temperature structure. This is then used in a radiative transfer model to predict brightness temperatures.

Microwave radiative transfer in lunar surface layers can generally be modelled with the use of multilayer models (Fung *et al*., 2006). Fa and Jin (2006) proposed a two-layer model composed of a lunar regolith layer and an underlying bedrock layer. Fa and Jin (2007) also developed a three-layer model, which includes a top dust layer, a soil layer and an underlying bedrock layer. In both models it was assumed that the vertical temperature distribution in the same layer is homogeneous and the dielectric permittivity is constant. Both models, then, used the strong fluctuation random medium theory to calculate the subsurface TB of each layer. Vasavada *et al*. (1999), Lan and Zhang (2004), and Meng (2008) also used two-layer models and combined them with ground-based radar data of lunar poles to derive upper lunar regolith thickness.

The two-layer and three-layer models are simple stratifications of important parameters (e.g. density, permittivity, and conductivity) that affect the TB. However, such simplified stratification can also cause problems. For example, the Vasavada *et al*. (1999) two-layer model predicts larger temperature values during the daytime for areas with a large lunar regolith thickness (e.g. 2 m or more) than the temperature values measured by the Diviner radiometer, whereas the model simulated temperatures at night-time is predicted to be smaller than the actual temperatures measured by Diviner (Bandfield *et al*., 2011). There is trade off with the number of layers in the model and the accuracy of the model. The larger the number of the layers, the longer the computational time of the model, but the greater the potential accuracy.

For a thermal microwave emission model, the dielectric profile of the upper lunar regolith is very important as it changes the amount of microwave radiation adsorbed. The dielectric constant is dependent on the density of the lunar soil which changes rapidly in the lunar soil layer with depth (see section 3.2.). It is, thus, important to have enough layers in a thermal microwave emission model to capture this change in the dielectric constant. In the two-layer models (Vasavada *et al*., 1999; Lan and Zhang, 2004; Fa and Jin, 2006; Meng, 2008), the dielectric properties of the lunar regolith are simplified, with an approximate average dielectric constant, instead of the dielectric profile of the lunar regolith layer. The simulated TB from these two layer models will, then, produce errors due to this over simplification. So, the dielectric constant should be modelled to a greater accuracy than the reported two- and three-layer models.

Although the three-layer model (Fa and Jin, 2007) is an improvement compared with the two-layer model, by considering the density and thermal property differences between top 2-cm dust layer and lunar soil beneath it, the three-layer model is still too simple to simulate the parameters affecting TB, as shown in Fig. 7.

Fig. 7 shows that the TB simulated by the three-layer and two-layer models are remarkably different, in the two-layer model TB changes do not happen rapidly enough in the top 50 cm of the lunar surface when compared to data from the Apollo heat flow experiments. Even after a depth of 20 m the TB is still changing which is not supported by lunar soil lab simulation experiments (Zhang *et al*., 2009).

Theoretical and simulation results show that the three-layer model error (deviation with *in-situ* measurements and observations) is smaller than that of the simple two-layer model, and, therefore, has better stability (e.g. smaller differences between simulated 1 m depth temperature at day and night). Clearly with a larger number of layers the model has better accuracy, however, at a cost of greater computational time and more unconstrained parameters.

A detailed multi-layer model can more accurately reflect the change in the parameters with depth (e.g. density, permittivity, conductivity) and obtain good results. However, the computing

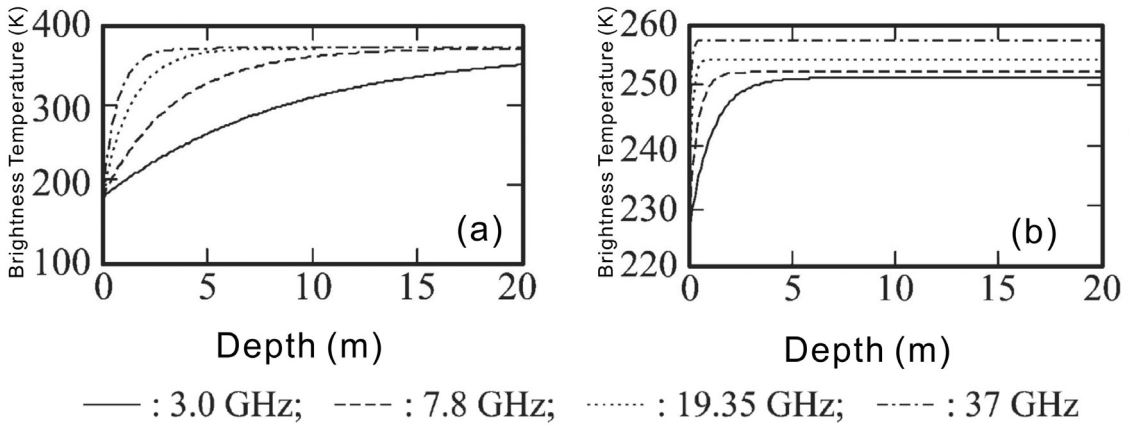

Fig. 7 - The midday TB at equatorial regions (note: as previously defined, TB is not the real surface temperature), as simulated on the basis of the: a) two-layer (Vasavada *et al*., 1999) and b) three-layer (Fa and Jin, 2006) models, respectively. Curves are derived on the basis of layers setup in Vasavada *et al*. (1999) and Fa and Jin (2006), as the Vasavada *et al*. (1999) model itself is a thermal diffusion model which did not predict TB. Both models are theoretical calculations, which do not involve real MRM data. The actual temperature profile is closer to model b, while there is no more difference between models a and b besides the difference in number of layers.

complexity will increase proportional to the number of layers, which will complicate the inversion of lunar subsurface temperature. Therefore, we should consider the instrument details and number of available microwave channels to make a compromise before the construction of a model.

3.5.2. Six-layer thermal diffusion simulation model

All four MRM channels should be included to invert the MRM data effectively, and, therefore, this model should be a multilayer model (assuming that each channel has a different maximum penetration depth). However, a trade off exists with complexity. Hence, a total of six layers are considered in the model, as follows: the top 2-cm lunar dust layer, followed by four layers between 2 cm and 5 m (with a greater number of layers in the top 20 cm where the temperature changes most rapidly) and a deepest layer at 5 m (bedrock layer). The depth of four layers between 2 cm and 5 m was set by taking into account the predicted penetration depth of each of the four MRM channels using a nominal lunar soil composition. Hence the following stratification is used:

$$Zarr = \begin{cases} 2, \textit{lunar dust } d_1 \\ 3, \textit{lunar soil } d_2 \\ 5, \textit{lunar soil } d_3 \\ 10, \textit{lunar soil } d_4 \\ 480, \textit{lunar soil } d_5 \\ \textit{Infinity, lunar regolith } d_6. \end{cases} \tag{7}$$

In the model, *Zarr* is the array of depths from the surface to base of each layer (not layer thicknesses) in centimetres, and *z* is the symbol representing depth in this work. An illustration is plotted in Fig. 8.

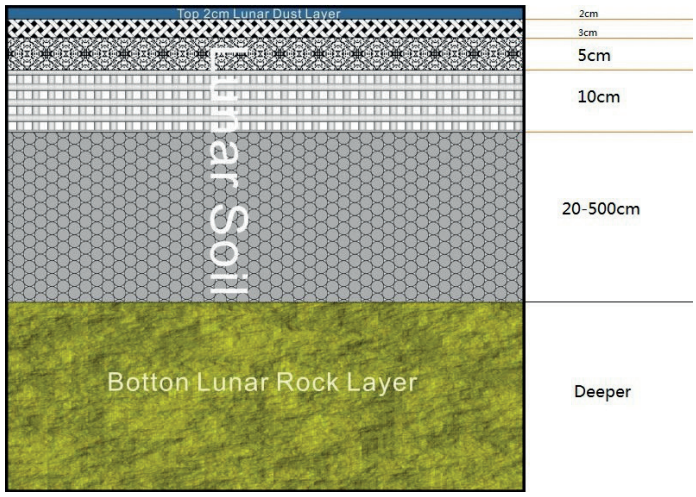

Fig. 8 - Lunar soil layers for the thermal simulation model (which will also be used in the microwave radiative transfer model, section 4.2.).

Prior to constructing the forward model, a calculation of the vertical temperature distribution is made to test this six-layer stratification. The calculation, which is mainly based on the code described by Spencer *et al*. (1989), is a 1D numerical thermal model written in IDL. The code calculates the surface and subsurface temperatures on a rotating body as a function of local time. Documentation of the basic model can be found in Spencer *et al*. (1989) and is subsequently referred to as the 'Spencer' code in this work.

The Spencer code is based on an equilibrium model (EQM). Spencer *et al*. (1989) suggested the following:

1. a set of standard thermal model equations:

$$\begin{cases} \eta\varepsilon\sigma T_{SS}^4=(1\text{-A})S_1 / R^2 \\ T = T_{SS}\cos^{1/4}\varphi,\ \varphi \le \pi/2 \\ T = 0,\ \varphi \le \pi/2 \end{cases} \tag{8}$$

   where T is the temperature, φ is the latitude, ε is the bolometric emissivity, σ is the Boltzmann's constant, η is an empirical beaming factor, A is the bolometric albedo, S is the solar constant at 1 AU, and R is the heliocentric distance in AU;

2. the model obtains the temperature T as a function of depth below the surface z and time t by numerically solving the 1D thermal conductive heat flow equation, as follows:

$$\rho c\frac{\partial T(z,t)}{\partial t} = \frac{\partial}{\partial z}\left[k\frac{\partial T(z,t)}{\partial t}\right] \tag{9}$$

   where ρ is the density, c is specific heat capacity and k is the thermal conductivity.

Spencer *et al*. (1989) original use for the model is rapidly rotating asteroids, so for this calculation the parameters are adapted for the Moon. The equation is evaluated over the z interval from 0, at the surface, to some depth d. Setting: the albedo to a lunar value of 0.14 (Spencer *et al*., 1989), the emissivity to a lunar value of 0.94 (Spencer *et al*., 1989), the time increments to ~250 s, the number of runs for energy balance to 50 (after 50 runs the results are almost identical, i.l. <1% difference), and the distance to the Sun to 1 AU. The temperature profile reported in Fig. 9 is obtained.

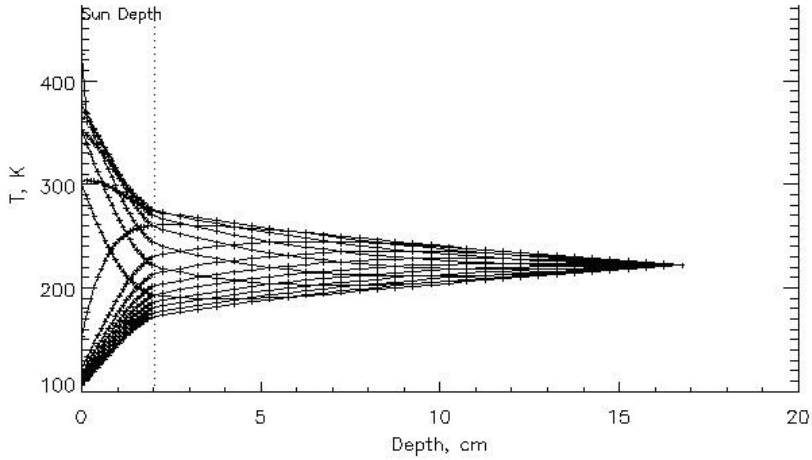

Fig. 9 - Calculated depth profile of mean temperature at various local times (from midday to midnight). Heat conductivity *k* values from section 3.3 were used. After 17 cm the subsurface temperature converges to an almost constant value, due to the penetration limit of sunlight. And this is consistent with the Vasavada *et al*. (1999) model results shown in Fig. 6. The vertical resolution in this calculation is 0.1 cm, while the "Sun depth" means the depth that sunlight could affect to.

Fig. 9 shows that the lunar surface temperature around the equator varies significantly in the upper 17 cm. At the surface the hottest temperature can reach up to 380 K during lunar daytime, while the coldest can be 100 K during lunar nights. This compares well with the Diviner observations of lunar surface *(*Paige *et al*., 2010). Diviner measures the maximum temperature at equatorial regions as 380 K and the minimum temperature is found to be 100 K.

4. Subsurface microwave radiative transfer model

Although some preliminary results were derived in section 2, these only represent a qualitative first order analysis of the Chang'E (CE) MRM data, for lunar subsurface temperature sounding. To fully exploit the measurements made by the MRM instrument and future microwave radiometers, the establishment of a lunar regolith microwave radiative transfer forward model is required. This will allow quantitative insights into the subsurface temperature and compositional structure to be included when interpreting the MRM data. In turn, this is the key to exploiting the information on subsurface heat flow and its possible connection to the large-scale evolution of the lunar crust.

By considering the main factors affecting the measured brightness temperature with depth within the lunar regolith, I have developed a non-uniform multi-layer lunar soil radiative transfer model. This new model is entirely different to the models of Spencer *et al*. (1989) or Vasavada *et al*. (1999), because it is not an energy balance (thermal diffusion) model, but a microwave radiative transfer model using input data from the MRM measurements, effectively modelling the global subsurface radiative transfer for the time of the remote sensing observation. According to microwave radiative transfer theory (Ulaby *et al*., 1981; Jin, 1998), the CE MRM measurements of lunar regolith contain TB contributions from different layers within a certain depth of the subsurface. Physical properties of different depths of lunar soil,

such as different temperature, dielectric constant, density, thermal conductivity, and specific heat parameters, will be reflected in the microwave radiation transport model and thus the TB measured by the instrument.

The radiative transfer forward model is used to calculate contributions from different depths to the TB measured by the MRM radiometer's four channels. This can then be compared with other models and methods such as Keihm *et al*. (1973) model or Spencer *et al*. (1989) one, assuming a known vertical temperature distribution. Furthermore, to try and understand if there is correlation with the Fe/Ti content and the effective emission depth for the different MRM channels, a sequence of more complex models investigating radiative and conductive heating measured by each of the MRM channels has been developed.

4.1. Radiative transfer forward model derivation

The first step in developing the thermal transfer model is determining the contributions from each layer to the subsurface microwave propagation that is, then, received by the instrument. In this initial analysis a six-layer model has been used for the reasons outlined in section 3.6.

The rationale for using a total of six layers is described in part 3, but to a first order is due to the number of available channels (4) of MRM data, assuming each channel is sounding to a different depth (section 2.1). The number of required layers is equal to the number of channels plus a top layer and a bottom layer. The top layer is constrained by the surface temperature data from the Diviner instrument on the Lunar Reconnaissance Orbiter (Paige *et al*., 2010) (i.e. layer 1), the four MRM channels potentially provide measurements at four different depths (i.e. layers 2 to 5) and the bedrock temperature can be considered as a constant (i.e. layer 6). This allows the number of unknowns to equal the number of equations, making the problem pseudo-exact due to the presence of measurement and modelling error.

Existing microwave propagation models developed for the Earth's subsurface are not appropriate. The microwave propagation in the Earth's subsurface is heavily attenuated by the presence of moisture (Jin, 1998; Zhang *et al*., 2008) so existing terrestrial models are not applicable for the analysis of data from desiccated airless bodies such as the Moon. Therefore, I have constructed my own model using underlying principles of microwave radiative transfer theory. This approach will be summarised below, with references to the individual model components cited as required unless it is an original derivation.

Any substance with a temperature above absolute zero has a large number of charged particles that constantly collide with one another, causing the charged particles to be in a state of motion. Such changes in motion (i.e. acceleration) generate electromagnetic radiation, and different frequencies of non-correlated wave components constitute emission of electromagnetic wave radiation. In electromagnetic terminology, the frequency range from 1000 MHz to 300 GHz is called microwave radiation (this will be Planck radiation modified by the material if it is not transparent to its own radiation).

A microwave radiometer is a high-sensitivity receiver designed to receive and record low emission random microwave noise[3] radiation from a material. Objects in thermodynamic

[3] 'Noise' in this case implies that the radiation is not coherent, in contrast, for example, to a microwave receiver as used in communications or similar.

equilibrium have an emission power (in radio frequency microwave language this is referred to as the transmission power) P, which is a function of their physical temperature T. In the microwave range, P is proportional to T (the long-wave limit of the Planck function) (Ulaby *et al*., 1981). This is expressed as:

$$P = \sigma\, eT\Delta\nu \tag{10}$$

where σ is the Boltzmann constant, T is the thermodynamic temperature of the object, e is the emissivity of the material, and $\Delta\nu$ is the radiometer bandwidth. This relationship between power and temperature defines the T_B, which is characterised by the power received in a real scene:

$$T_B = eT = \frac{P}{\sigma\Delta\nu}\ . \tag{11}$$

Since e (the emissivity of the material) is dependent on the dielectric constant, it is also dependent on density and elemental composition, etc. The observed microwave TB is, thus, dependent on these characteristics (e.g. density, elemental composition, etc.), so we could, in principle, derive these lunar subsurface parameters, based on the MRM remote measurements of lunar surface brightness temperature using Eq. 11.

Fig. 10 is a schematic diagram of the microwave radiation from a typical three-layer lunar regolith and bedrock structure (after Li *et al*., 2010). In addition to the microwaves being attenuated by medium during their propagation through the lunar surface, they will also be affected by changes in the medium. For example, if the lunar regolith comprises three layers with different dielectric properties and temperatures (T0, T1, T2, T3), then the emitted microwave radiation from each layer will be affected by reflection and transmission at every interface.

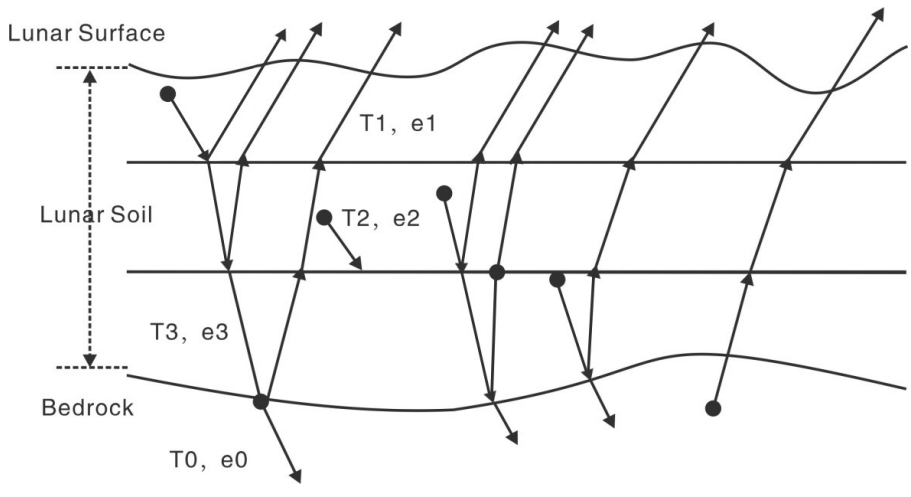

Fig. 10 - Schematic diagram of microwave radiation emitted from a three-layer lunar regolith and bedrock structure. The T_B received by the MRM contains direct emission from each layer, as well as reflected beams at layer interfaces, although multiple reflections will not be considered in this model.

The total amount of radiation received by the microwave detector from the lunar surface is expressed by (Ulaby *et al*., 1981) as:

$$T_B = T_S e_s = T_s\,(1-r_s) \tag{12}$$

where *Ts* is the thermodynamic temperature of the surface, e_s is the emissivity of the surface and r_s is the surface reflectivity. r_s can be calculated according to Fresnel's Law of reflection:

$$r_s = \left| \frac{\varepsilon_{rs}\cos\theta - \sqrt{\varepsilon_{rs} - \sin^2\theta}}{\varepsilon_{rs}\cos\theta + \sqrt{\varepsilon_{rs} - \sin^2\theta}} \right|^2 \tag{13}$$

where ε_{rs} is the relative permittivity of the surface.

In the case of normal incidence, the reflectivity then becomes:

$$r_s = \left| \frac{1-\sqrt{\varepsilon_{rs}}}{1+\sqrt{\varepsilon_{rs}}} \right|^2 \tag{14}$$

The subsurface temperature profile is given by $T(z)$, the absorption coefficient profile is $\alpha(z)$ and permittivity profile is $\varepsilon(z)$, all are functions of the depth z. The depth profile of the layer dielectric constant $\varepsilon(z)$ is given by Tsang *et al*. (1975) and the absorption coefficient profile of the electric field intensity $\alpha(z)$ is expressed as:

$$\alpha(\mathrm{z}) = \frac{2\pi}{\lambda}\left\{ \frac{\mu_r(\mathrm{z})\varepsilon'_r(\mathrm{z})}{2}\left[\sqrt{1+\left(\frac{\varepsilon''_r(\mathrm{z})}{\varepsilon'_r(\mathrm{z})} \right)^2} - 1 \right] \right\}^{1/2} \tag{15}$$

where λ is wavelength, ε'_r is the real part of the relative permittivity while ε''_r is the imaginary part, μ_r is the real part of the magnetic permittivity. The power absorption coefficient $\kappa(z)$ is twice that of $\alpha(z)$, as expressed by:

$$\kappa(z) = 2\,\alpha(z) \tag{16}$$

where the $\kappa(z)$ and $\alpha(z)$ units are both in nepers (Np) per metre (neper is defined as 1 Np/m=8.686dB/m). If the dielectric of each layer is the same and $\mu_r(z)$=1, then the absorption coefficient $k(z)$ can be expressed as:

$$\kappa(z) = 2\,\mathrm{Im}\left\{ \frac{2\pi\sqrt{\varepsilon_r(z) - \sin^2\theta}}{\lambda} \right\}. \tag{17}$$

We need to define a difference between real temperature, effective temperature and brightness temperature:

1. real temperature is the thermodynamic temperature of the regolith. This is the temperature that would be measured by an *in-situ* temperature probe. In this model it is assumed that each layer is isothermal at one real temperature;
2. the lunar surface is composed of many different temperatures i.e. across a horizontal 2-cm space on the lunar surface the temperature can vary by up to 100 K. As seen in section 3.6 the temperature in the subsurface of the Moon can vary by 150 K to depths of 5 m.

The MRM instrument can sound to depths of 5 m and its footprint is 18 km at its best resolution, so it contains a scene composed of many different temperatures both vertically and horizontally. The effective temperature can be thought of as the average temperature in such a scene;

3. brightness temperature is the effective temperature multiplied by the effective emissivity of lunar regolith as measured by a microwave radiometer.

The model calculates the real temperatures of each layer. The real temperature from each layer is then multiplied by a weighting which is the power coefficient and the exponential of the negative power coefficient (Eq. 18). The real temperature multiplied by the weighing coefficient for each layer is, then, added together to give the effective temperature (Eq. 18). This effective temperature is, then, multiplied by the effective emissivity to give the TB that is measured by the MRM instrument. Then, Eq. 11 transforms into Eq. 18:

$$T_B = eT = e_{eff} T_{eff} = e_{eff} \int_{-\infty}^{0} T(z)\kappa(z)e^{-\kappa(z)}dz \tag{18}$$

where T_{eff} is the effective temperature, e_{eff} is the effective emissivity and represents the ratio of T_{eff} to the T_B measured by MRM. Here the $\kappa(z)e^{-\kappa(z)}$ weighting term comes from the derivative of $exp(-\kappa(z))$.

Microwave radiation in the media can be simulated using two methods. The first is the coherent method based on Maxwell's equations and the fluctuation-dissipation theorem (FDT). The coherent method considers the effects of reflection on both the amplitude and phase. The coherent method must be solved using Maxwell's equations to calculate electromagnetic field vectors and obtain radiation intensity. This approach requires that the medium is uniform as the scattering within each layer is ignored. The dielectric constant of each layer is also considered to be constant (Jin, 1998).

The second method is the incoherent approach based on the vector radiative transfer theory, which only considers the amplitude and not the phase. This approach requires a large amount of scattering bodies whose dimensions are comparable to the wavelength of radiation (Ulaby *et al*., 1981). The random distribution of such scattering bodies generates random phase functions in wave transmission between two points, thus making the transmission an incoherent process.

Considering the nature of the lunar soil (e.g. the layers are almost level and uniform and each layer has a constant dielectric constant) and the wavelengths measured by the MRM, the coherent method was chosen for this work. In coherent methods, the microwave radiation of the medium is caused by charged particles' fluctuating in the microscopic scale, that is, the fluctuant electromagnetic radiation. The expected relationship between the value of the electric current source (generated by the movement of charged particles) and TB is described by the FDT. Details of this theorem are explained in Jin (1998) and are summarised below.

The FDT relies on the assumption that the response of a system in thermodynamic equilibrium to a small-applied force is the same as its response to a spontaneous fluctuation[4]. Therefore, the theorem connects the linear response relaxation of a system from a prepared non-equilibrium state to its statistical fluctuation properties in equilibrium. According to FDT:

$$(\bar{J}_l(\bar{r},\omega) * \bar{J}_l(\bar{r}',\omega')) = \frac{4}{\pi}\omega\varepsilon_l''(z)\sigma T_l(z)\cdot\bar{I}\,\delta(\omega-\omega')\delta(r-r') \tag{19}$$

[4] Another example is Einstein's model of Brownian motion, also a use of FDT and derivation of refractive index.

where $\bar{J}_l(\bar{r},\omega)$ is the heat source of layer l among all N layers, ω is the heat radiation's angular frequency, r is the displacement vector, σ is the Boltzmann constant, and $T_l(z)$ is the real temperature distribution of layer l, $\varepsilon''_l(z)$ is the imaginary part of permittivity (dielectric constant), the term I in Eq. 19 is defined as:

$$\bar{I} = \hat{x}\hat{x} + \hat{y}\hat{y} + \hat{z}\hat{z}. \tag{20}$$

Therefore, by the definition of TB and Eqs. 18 to 20, the polarised radiation TB can be written as:

$$T_B^p(\hat{k},\omega) = \frac{(2\pi)^3}{B}\left(\frac{c}{\omega}\right)\frac{1}{2}c\varepsilon_0\int_0^\infty d\omega'\int_0^\infty k^2 dk\int dk' \times \left\{\hat{p}\cdot\left(\bar{E}(k,\omega)\bar{E}'(k',\omega')\right)\cdot\hat{p}\exp[i(\bar{k}-\bar{k}')\cdot(r-i(\omega-\omega')t)]\right\} \tag{21}$$

where $\hat{p}$ is the polarisation sense, $\hat{p} = (\hat{v}, \hat{h})$, $\hat{h}$ is the horizontal polarisation vector, $\hat{v}$ is the vertical polarisation vector, c is the light speed, ω is the frequency, r is the distance vector, and ε_0 is the vacuum relativity. Also, by using the parallel-layered media dyadic Green's function (Jin, 1998) the electric field intensity (E) can be written as:

$$\bar{E}\left(\vec{r},\omega\right) = \sum_{l=1}^{N+1}\int_{-\infty}^{\infty} d\bar{\rho}'\int_{-d_l}^{-d_{l-1}} dz'\overline{\overline{G}}_{0l}\left(\bar{r},\bar{r}'\right)\bullet J_l\left(\bar{r}'\right)\omega' \quad . \tag{22}$$

In Eq. 22, J_l is the heat source, ρ is the x-y plane; the lth layer-represents the longitudinal coordinates of the lth layer; dyadic Green function in the region l can be written as:

$$\begin{aligned}&\overline{\overline{G_{0l}}}\left(\bar{r},\bar{r}'\right) = -\frac{\omega\mu}{8\pi^2}\int d\bar{k}\,\delta\left[k_z - \sqrt{\omega^2\mu\varepsilon_0 - k_\rho^2}\right]\frac{1}{k_z}e^{i\bar{k}\bullet\bar{r}}\times \\ &\left\{\hat{h}(k_z)\left[A_l\hat{h}(-k_{lz})e^{-i\bar{k}\bullet\bar{r}} + B_l\hat{h}(k_{lz})e^{-i\bar{k}\bullet\bar{r}}\right] + \hat{v}(k_z)\left[C_l\hat{v}(-k_{lz})e^{-i\bar{k}\bullet\bar{r}} + D_l\hat{v}(k_{lz})e^{-i\bar{k}\bullet\bar{r}}\right]\right\}\end{aligned} \tag{23}$$

where subscript 0l indicates that the observation point $\bar{r}$ is in area 0 and the microwave emission source is located in area l. k_ρ is the wavenumber on the x-y plane, k_x is the wavenumber projected into the x axis and k_y is the wavenumber projected into the y axis, $k_\rho^2 = k_x^2 + k_y^2$. μ is the vacuum magnetic permittivity; A_l, B_l, C_l and D_l can be derived by tangential continuous boundary constraints at layer interfaces. For an N-layer unevenly paralleled dissipation medium, when the observation angle is θ, the zero-order p-polarisation TB of layered lunar soil medium measured by MRM can be transformed into Eq. 24:

$$\begin{aligned}&T_B^p(\theta) = \frac{k_0}{\cos\theta}\sum_{i=1}^{n}\left\{\frac{\varepsilon''_{ri}}{2k''_{iz}}\left|\beta_i^p\right|^2\cdot\left(1-e^{-2k''_{iz}d_i}\right)\cdot\left(1+\left|R_{i(i+1)}^p\right|^2 e^{-2k''_{iz}d_i}\right)T_i\prod_{j=0}^{i=1}\left(\left|Q_{j(j+1)}^p\right|^2\cdot\left(e^{-2k''_{jz}d_j}\right)\right)\right\} + \\ &\frac{k_0\varepsilon''_{r(n+1)}\left|\beta_{n+1}^p\right|^2}{\cos\theta\cdot 2k''_{(n+1)z}}\cdot\prod_{j=0}^{n}\left(\left|Q_{j(j+1)}^p\right|^2\cdot\left(e^{-2k''_{jz}d_j}\right)\right)T_r\end{aligned} \tag{24}$$

where k is the wavenumber, k_{iz} is the projection on z direction of the i layer's wavenumber, d_i is the thickness of the i layer, T_r is the temperature of the lunar rock layer, and the superscript '' means the imaginary part. The transmission coefficient (Q_{ij}) is:

$$Q_{ij} = 1 + R_{ij} \tag{25}$$

And the reflection coefficient is:

$$R_{ij} = \frac{k_{iz} - k_{jz}}{k_{iz} + k_{jz}} . \tag{26}$$

Therefore, for a six layer non-uniform parallel layered dissipative media, when the observation angle is zero, as in the CE MRM data, based on Eq. 24, the layered medium polarised radiation brightness temperature measured by the microwave radiation detector can be deduced as:

$$\begin{aligned}
T_B = {} & \frac{k_0 \varepsilon_1^{''}}{2\varepsilon_0 k_1^{''}} \left|Q_{01}\right|^2 (1 - e^{-2k_1^{''}d_1})(1 + \left|R_{12}\right|^2 e^{-2k_1^{''}d_1}) T_1 \\
& + \frac{k_0 \varepsilon_2^{''}}{2\varepsilon_0 k_2^{''}} \left|Q_{01}Q_{12}\right|^2 (1 - e^{-2k_2^{''}d_2})(1 + \left|R_{23}\right|^2 e^{-2k_2^{''}d_2}) e^{-2k_1^{''}d_1} T_2 \\
& + \frac{k_0 \varepsilon_3^{''}}{2\varepsilon_0 k_3^{''}} \left|Q_{01}Q_{12}Q_{23}\right|^2 (1 - e^{-2k_3^{''}d_3})(1 + \left|R_{34}\right|^2 e^{-2k_3^{''}d_3}) e^{-2k_1^{''}d_1} e^{-2k_2^{''}d_2} T_3 \\
& + \frac{k_0 \varepsilon_4^{''}}{2\varepsilon_0 k_4^{''}} \left|Q_{01}Q_{12}Q_{23}Q_{34}\right|^2 (1 - e^{-2k_4^{''}d_4})(1 + \left|R_{45}\right|^2 e^{-2k_4^{''}d_4}) e^{-2k_1^{''}d_1} e^{-2k_2^{''}d_2} e^{-2k_3^{''}d_3} T_4 \\
& + \frac{k_0 \varepsilon_5^{''}}{2\varepsilon_0 k_5^{''}} \left|Q_{01}Q_{12}Q_{23}Q_{34}Q_{45}\right|^2 (1 - e^{-2k_5^{''}d_5})(1 + \left|R_{56}\right|^2 e^{-2k_5^{''}d_5}) e^{-2k_1^{''}d_1} e^{-2k_2^{''}d_2} e^{-2k_3^{''}d_3} e^{-2k_4^{''}d_4} T_5 \\
& + \frac{k_0 \varepsilon_6^{''}}{2\varepsilon_0 k_6^{''}} \left|Q_{01}Q_{12}Q_{23}Q_{34}Q_{45}Q_{56}\right|^2 e^{-2k_1^{''}d_1} e^{-2k_2^{''}d_2} e^{-2k_3^{''}d_3} e^{-2k_4^{''}d_4} e^{-2k_5^{''}d_5} T_6
\end{aligned} \tag{27}$$

This Eq. 27 is the core of the model. Each term in this equation corresponds to a layer's contribution to the received TB (of specific wavelength) and is calculated based on Eq. 24. The first term corresponds to the lunar dust layer's radiation and the last term corresponds to the lunar bedrock layer's radiation, while the other four terms correspond to each layer of the lunar soil. Except for the last term, all the other five terms contain both upward radiation and downwards reflected radiation. Eq. 27 calculates the zero-order radiation TB, e.g. the effect of scattering is not considered. Other assumptions include: T_6=250 K (bedrock temperature), the vacuum permittivity is unity and the bedrock layer permittivity is 8.0+0.5*i* (Heiken *et al*., 1991). To determine the wavenumber k, we can write:

$$k = \frac{\omega}{c}(\beta + i\alpha) . \tag{28}$$

Then, according to Burke *et al*. (1979), the dispersion relation gives:

$$\beta = \left\{ \frac{1}{2} (\varepsilon_{RJ} - \sin^2 \theta_0)[1 + (1 + \frac{\varepsilon_{Ij}^{\ 2}}{(\varepsilon_{RJ} - \sin^2 \theta_0)^2})^{1/2}] \right\}^{\frac{1}{2}} \tag{29}$$

$$\alpha = \frac{\varepsilon_I}{2\beta} . \tag{30}$$

Eqs. 25 and 26 are widely used in microwave remote sounding including moisture estimation

of terrestrial soil (Zhang *et al*., 2008). Eqs. 28 to 30 are also used in the inversion model developed in paper to allow estimation of *k*.

4.2. Forward model calculation

In this paper the sum of TiO_2 content (%) and FeO content (%) on the lunar surface is denoted as S (%). The MRM measured temperature depth profile of the lunar surface is dependent on the value of S and its variation with depth. The MRM observed TB (T_B) could be calculated from Eq. 27; each term in Eq. 27 corresponds to each layer's contribution; T_1, T_2, ... T_6 represent the real temperature of each layer.

Here T_1 is provided from the Diviner mission data product (Paige *et al*., 2010). T_6 is set as 250 K constrained by the Apollo measurements (Heiken *et al*., 1991), hence only T_2-T_5 are unknowns.

The initial tests of the forward model behaviour used the theoretical values of T_2-T_5 derived from Fig. 8 using the Spencer *et al*. (1989) model to calculate the 'expected' and synthetic MRM TB for all four channels, using each subsurface layer's 'approximate' energy contribution. Then, in the inverse model steps, the measured TB values from the MRM data product will be used to estimate values for T_2-T_5. Both the model and inverse algorithms have been coded in MATLAB/Fortran and example calculation runs are described below.

Using the expected values for the lunar subsurface temperatures from section 3.6, the forward model results are derived, see Fig. 11. When S=10 (i.e. close to lunar average FeO and TiO_2), radiance comes mainly from the deepest layer, especially for the 3 GHz channel and under these circumstances most contributions are from the 5th layer (50-500 cm).

As the lunar highlands typically have a low S value (1-5) (Heiken *et al*., 1991), from Fig. 11, one can use 3 GHz as the deep layer temperature (50 cm-5 m).

4.3. Inverting vertical subsurface temperatures of the equatorial region from MRM data and using the microwave forward model

The lunar subsurface is not isothermal, so the microwave radiation of the lunar surface is also affected by the actual temperature distribution of the subsurface of the Moon. By solving the radiation transmission equations (Eqs. 10 to 30), this paper will establish a lunar subsurface temperature inversion model, using the CE MRM measurements. To study the typical vertical distribution of the lunar subsurface temperature, this work will use the analytical microwave radiative transfer model to attempt an inversion of the equatorial region subsurface temperatures at different depths, based on the MRM data (section 4.1).

What MRM 'measured' is, then, numerically studied: using the inverse method to retrieve the subsurface temperatures (T_2-T_5), defined as the unknown matrix x in the following discussion. To setup the basic equations for the inversion, the measurement vector should be the 4 MRM measured brightness temperatures in each channel, e.g. TB1 (3.0 GHz), TB2 (7.8 GHz), TB3 (19.35 GHz), TB4 (37.0 GHz), each with a measurement error of ±0.5 K, respectively. The unknown vector x should be made of the real sub-surface temperatures, T_2 (5 cm), T_3 (10 cm), T_4 (20 cm), and T_5 (2 m).

According to the inverse method (e.g. Rodgers, 2000), the measurement vector (y) is equal to the vector of unknowns (x) multiplied by the weighting function matrix (**K**) plus the error matrix (y=**K**·x+error). The matrix of unknowns is defined by x=[T_2, T_3, T_4, T_5], y is defined as

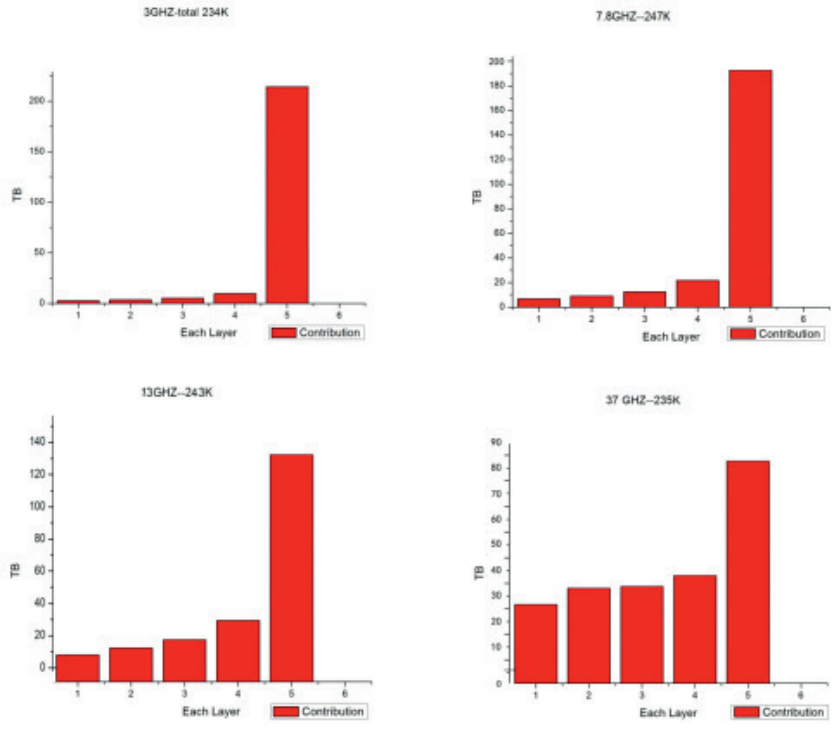

Fig. 11 - Each layer's weight (contribution) in the CE-1 and CE-2 MRM brightness temperature measurements (when S=10), with the measured MRM brightness temperature marked on the top. With the lunar average S value being close to 10, we can see that the MRM data is close to the forward model's prediction (234 K, 235 K), which validated this forward model.

below in Eq. 31 derived from Eq. 27, which is the net TB contribution of each lunar soil layer excluding the contribution of dust and rock layer to TB. The dust and rock layer are excluded due to the fact that values of T_1 (Diviner data) and T_6 are known [250 K, Apollo measurement (Heiken *et al*., 1991)], making the contribution from these two layers calculable:

$$y = \begin{bmatrix} TB_1 - CTB_{3GHz} \\ TB_2 - CTB_{7.8GHz} \\ TB_3 - CTB_{19GHz} \\ TB_4 - CTB_{37GHz} \end{bmatrix} = \begin{bmatrix} TB_1 - (\frac{k_0\varepsilon_1''}{2\varepsilon_0 k_1''}|Q_{01}|^2(1-e^{-2k_1''d_1})(1+|R_{12}|^2 e^{-2k_1''d_1})T_1 \\ -\frac{k_0\varepsilon_6''}{2\varepsilon_0 k_6''}|Q_{01}Q_{12}Q_{23}Q_{34}Q_{45}Q_{56}|^2 e^{-2k_1''d_1}e^{-2k_2''d_2}e^{-2k_3''d_3}e^{-2k_4''d_4}e^{-2k_5''d_5}T_6)_{3.0GHz} \\ TB_2 - (\frac{k_0\varepsilon_1''}{2\varepsilon_0 k_1''}|Q_{01}|^2(1-e^{-2k_1''d_1})(1+|R_{12}|^2 e^{-2k_1''d_1})T_1 \\ -\frac{k_0\varepsilon_6''}{2\varepsilon_0 k_6''}|Q_{01}Q_{12}Q_{23}Q_{34}Q_{45}Q_{56}|^2 e^{-2k_1''d_1}e^{-2k_2''d_2}e^{-2k_3''d_3}e^{-2k_4''d_4}e^{-2k_5''d_5}T_6)_{7.8GHz} \\ TB_3 - (\frac{k_0\varepsilon_1''}{2\varepsilon_0 k_1''}|Q_{01}|^2(1-e^{-2k_1''d_1})(1+|R_{12}|^2 e^{-2k_1''d_1})T_1 \\ -\frac{k_0\varepsilon_6''}{2\varepsilon_0 k_6''}|Q_{01}Q_{12}Q_{23}Q_{34}Q_{45}Q_{56}|^2 e^{-2k_1''d_1}e^{-2k_2''d_2}e^{-2k_3''d_3}e^{-2k_4''d_4}e^{-2k_5''d_5}T_6)_{19.0GHz} \\ TB_4 - (\frac{k_0\varepsilon_1''}{2\varepsilon_0 k_1''}|Q_{01}|^2(1-e^{-2k_1''d_1})(1+|R_{12}|^2 e^{-2k_1''d_1})T_1 \\ -\frac{k_0\varepsilon_6''}{2\varepsilon_0 k_6''}|Q_{01}Q_{12}Q_{23}Q_{34}Q_{45}Q_{56}|^2 e^{-2k_1''d_1}e^{-2k_2''d_2}e^{-2k_3''d_3}e^{-2k_4''d_4}e^{-2k_5''d_5}T_6)_{37.0GHz} \end{bmatrix} \quad (31)$$

where CTB is the contribution of dust and rock layer to the TB measured by the MRM instrument. Note that the CTB is a known quantity as it is set by Diviner and Apollo measurements. Q is the transmission coefficient (Eq. 25) and R is the reflection coefficient (Eq. 26).

According to the temperature uncertainty of the MRM instrument (±0.5 K) given in Table 1, the measurement uncertainty covariance matrix is then:

$$S_\varepsilon = \begin{bmatrix} 0.25 & 0 & 0 & 0 \\ 0 & 0.25 & 0 & 0 \\ 0 & 0 & 0.25 & 0 \\ 0 & 0 & 0 & 0.25 \end{bmatrix} \tag{32}$$

where the diagonal elements are given as the square of the error of the MRM instrument. And according to Eq. 27, the weighting function matrix is:

$$K = \begin{bmatrix} C^{Second}_{3.0\times10^9\,GHz} & C^{Third}_{3.0\times10^9\,GHz} & C^{Forth}_{3.0\times10^9\,GHz} & C^{Fifth}_{3.0\times10^9\,GHz} \\ C^{Second}_{7.8\times10^9\,GHz} & C^{Third}_{7.8\times10^9\,GHz} & C^{Forth}_{7.8\times10^9\,GHz} & C^{Fifth}_{7.8\times10^9\,GHz} \\ C^{Second}_{19.0\times10^9\,GHz} & C^{Third}_{19.0\times10^9\,GHz} & C^{Forth}_{19.0\times10^9\,GHz} & C^{Fifth}_{19.0\times10^9\,GHz} \\ C^{Second}_{37.0\times10^9\,GHz} & C^{Third}_{37.0\times10^9\,GHz} & C^{Forth}_{37.0\times10^9\,GHz} & C^{Fifth}_{37.0\times10^9\,GHz} \end{bmatrix} \tag{33}$$

where:

$$C^{Second} = \frac{k_0 \varepsilon_2''}{2\varepsilon_0 k_2''} \left|Q_{01}Q_{12}\right|^2 (1 - e^{-2k_2''d_2})(1 + \left|R_{23}\right|^2 e^{-2k_2''d_2}) e^{-2k_1''d_1} \tag{34}$$

$$C^{Third} = \frac{k_0 \varepsilon_3''}{2\varepsilon_0 k_3''} \left|Q_{01}Q_{12}Q_{23}\right|^2 (1 - e^{-2k_3''d_3})(1 + \left|R_{34}\right|^2 e^{-2k_3''d_3}) e^{-2k_1''d_1} e^{-2k_2''d_2} \tag{35}$$

$$C^{Forth} = \frac{k_0 \varepsilon_4''}{2\varepsilon_0 k_4''} \left|Q_{01}Q_{12}Q_{23}Q_{34}\right|^2 (1 - e^{-2k_4''d_4})(1 + \left|R_{45}\right|^2 e^{-2k_4''d_4}) e^{-2k_1''d_1} e^{-2k_2''d_2} e^{-2k_3''d_3} \tag{36}$$

$$C^{Fifth} = \frac{k_0 \varepsilon_5''}{2\varepsilon_0 k_5''} \left|Q_{01}Q_{12}Q_{23}Q_{34}Q_{45}\right|^2 (1 - e^{-2k_5''d_5})(1 + \left|R_{56}\right|^2 e^{-2k_5''d_5}) e^{-2k_1''d_1} e^{-2k_2''d_2} e^{-2k_3''d_3} e^{-2k_4''d_4} \tag{37}$$

According to the inverse theory (Rodgers, 2000):

$$x = (K^T S_\varepsilon^{-1} K)^{-1} K^T S_\varepsilon^{-1} y \tag{38}$$

and expression for the error covariance of the state x vector is:

$$S_x = (K^T S_\varepsilon^{-1} K)^{-1} \tag{39}$$

the vector of unknowns (x) and its associated error covariance (S_x) can therefore be estimated. However, this S_x is the model calculation error, without the parameter modelling error included.

A simple test of Eq. 38 was done to generate a vertical temperature profile for the lunar equator. When assuming a value of S=15 [typical for the lunar equatorial region, according to

(Heiken *et al*., 1991)], a rough average subsurface temperature curve for the Moon's equatorial region can be generated using the radiative transfer model and inverting the equatorial MRM data (Fig. 12). The surface temperature points are constrained by Diviner measurements (Paige *et al*., 2010). The stated error of the Diviner data is within ±2 K (Paige *et al*., 2010). The bedrock temperature is taken from the Apollo experiment with ±10 K error (Heiken *et al*., 1991) and the other points have been derived from the CE MRM measurements. Error is within ±6 K. The model shows that the lunar soil temperature changes significantly within the top 2 cm, and becomes stable below 20 cm. Comparing it with the theoretical thermal simulations in section 3.7, part 3, we notice that they agree to within the stated uncertainties. The data used for this forward model calculation is summarised in Table 2.

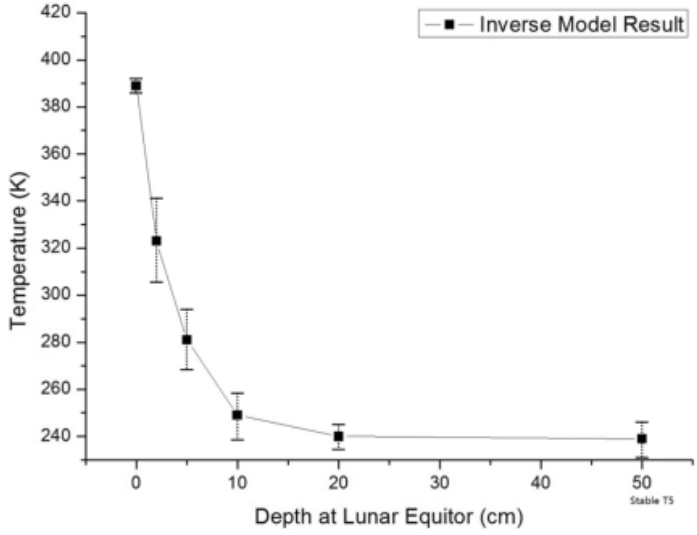

Fig. 12 - Based on CE-1 MRM data and my radiative transfer model, the "measured" mean vertical temperature profile beneath the lunar equatorial surface, at the lunar midday, was inverted.

Table 2 - Data used in forward model calculation is an average of CE-1 and CE-2, details are given in this table.

	CE-1 Microwave Brightness Temperature Dataset	CE-2 Microwave Brightness Temperature Dataset
Size details	346MB	992MB
Time Span	2007.11.27 - 2008.06.30	2010.10.15 - 2011.05.20
Space Resolution	3 GHz channel space resolution is 50 km. All other channels had a spatial resolution of ~35 km	3 GHz channel space resolution is 25 km. All other channels had a spatial resolution of ~17.5 km

Both the thermal simulation (section 3.6) and the MRM data (Fig. 12) show that the surface temperature at the lunar equator at noon is ~390 K and drops significantly within 20 cm, then is almost stable at ~240 K at depths below 20 to 50 cm. This is also described in the lunar source book [220<T<255 K (Heiken *et al*., 1991)].

In the model covariance matrix, it was noticed that the first three off-diagonal elements are quite large (e.g. +/-20 K), but the fourth off-diagonal element (T_5 error) was below 2-10 K. This is because, as shown in Fig. 11, the MRM signal mainly comes from the lunar soil at a depth of >50 cm.

5. Conclusion and discussions

The lunar soil temperature profile and subsurface heat flow are important parameters in lunar exploration. Modelling the heat flow of the Moon is an important part of the diagnostic tests of thermal evolution models. This measurement can also help to constrain the Moon's crustal composition of radioactive elements and give clues to its differentiation.

The lunar surface temperature has been measured using the Diviner lunar radiometer. However, the subsurface temperature had only been measured directly at the Apollo 15 and 17 landing sites before the launch of CE-1. The CE-1 and CE-2 lunar orbiters were each equipped with a four-channel MRM instrument. The MRM can detect the brightness temperature of the lunar surface to retrieve subsurface lunar regolith temperatures and other related properties.

In this paper, we first validated the MRM measurements, the near-surface TB measurements from MRM were compared to the near-surface temperature measurements made by Diviner. From the initial TB map of the CE MRM data, a unique 3 GHz (5 m subsurface depth) TB elevation in the Oceanus Procellarum region was observed. It was hypothesised that this elevation in subsurface temperature could be due to the presence of radioactive KREEP materials.

Then, we provided a lunar soil model, and derived vertical temperature profile of the Moon. Analytical expressions for the thermal physical parameters required in the 1D thermal diffusion models were derived from *in-situ* Lunar and Apollo measurements and laboratory measurements of returned samples. The Apollo measured temperature profile beneath the lunar surface matched well with the curve provided by the theoretical model simulations. The combination of CE MRM and Diviner data, as well as the theoretical model simulation, shows that the lunar surface temperature profile varies mainly within the top 20 cm, slightly within the top 20-50 cm (Vasavada *et al*., 1999) and is almost stable under 2 m depth.

Finally, using the parameters derived in the previous step for the 1D thermal diffusion model, a microwave radiative transfer model was established to interpret the MRM data according to the coherent approach of microwave transmission theory and FDT. To test the forward model, the predicted TB's contributions from different depths of the 4 channels were compared with the real MRM received TB data and were shown to be in good agreement. It was also discovered most of the information from the MRM measurements came from the temperature of the model's layer T_5 (depth 20-500 cm). Hence the error in the inverted temperatures of the other layers is much greater than the error in the derived temperature of T_5.

The regions with the low heating source have a 2 m subsurface temperature of approximately 240±4 K. This finding is in agreement (to within 3%) with the model used by Keihm *et al*. (1973), which did not consider radiogenic heating. While we observed that the average 2 m subsurface temperature in KREEP regions is higher. The KREEP region on the lunar surface contains the greatest abundance of uranium, thorium and potassium. The difference between the KREEP region and the non-KREEP is supported by Wieczorek's KREEP heat flow model (Wieczorek and Phillips, 2000), which predicts a 10 K difference between the KREEP centre and non-KREEP regions.

In future work, a global lunar heat flow model based on radiogenic element distribution will be built, to include other latitudes. In addition, like the Moon, the surfaces of the Mars also lacks water and vegetation. Therefore, a microwave sounding instrument, such as the MRM, also has applications on Mars and any other arid surface (e.g. asteroids). In future work,

possible improvements to the MRM instrument could be made to obtain a better inversion result. For example, current frequency selection is imperfect for subsurface temperature inversion of the Moon. A channel with 3 GHz can detect signals from a depth of several metres in the absence of moisture. However, the penetration depths of 19 and 37 GHz are quite close, i.e. 5 and 2 cm, respectively (Wang *et al*., 2010). Channel frequency selection and distribution should consider the target object type and its structure hierarchy.

Acknowledgements. Relevant data is free to download from the following website: http://moon.bao.ac.cn/ceweb/datasrv/dmsce1.jsp. CE-2 MRM data is free to download from: http://moon.bao.ac.cn/ceweb/datasrv/dmsce2.jsp and http://159.226.88.30:8080/CE2release/cesMain.jsp.

REFERENCES

Andrews-Hanna J.C., Besserer J., Head III J.W., Howett C.J.A., Kiefer W.S., Lucey P.J., McGovern P.J., Melosh H.J., Neumann G.A., Phillipps R.J., Schenk P.M., Smith D.E., Solomon S.C. and Zuber M.T.; 2014: *Structure and evolution of the lunar Procellarum region as revealed by GRAIL gravity data*. Nature, **514**, 68-71.

Bandfield J.L., Ghent R.R., Vasavada A.R., Paige D.A., Lawrence S.J. and Robinson M.S.; 2011: *Lunar surface rock abundance and regolith fines temperatures derived from LRO Diviner Radiometer data*. J. Geophys. Res., **116**, E00H02, doi: 10.1029/2011JE003866.

Braden S.E., Stopar J.D., Robinson M.S., Lawrence S.J., van der Bogert C.H. and Hiesinger H.; 2014: *Evidence for basaltic volcanism on the Moon within the past 100 million years*. Nature Geosci., **7**, 787-791, doi: 10.1038/NGEO2252.

Burke W.J., Schmugge T. and Paris J.F.; 1979: *Comparison of 2.8- and 21-cm microwave radiometer observations over soils with emission model calculations*. J. Geophys. Res., **84**, 287-294.

Cartier W.D., Mitchell J.K. and Mahmood A.; 1973: *The nature of lunar soil*. Journal of the Soil Mechanics and Foundations Division, **75**, 813-832.

Fa W.Z. and Jin Y.Q.; 2006: *Inversion of lunar regolith layer thickness using optical data and microwave emission simulation*. Chin. J. Radio Sci., **21**, 347-356, in Chinese.

Fa W.Z. and Jin Y.Q.; 2007: *Simulation of brightness temperature from lunar surface and inversion of regolith-layer thickness*. J. Geophys. Res., **112**, E05003.

Fa W. and Wieczorek M.A.; 2009: *Regolith thickness over the lunar nearside: results from Earth-based 70-cm Arecibo radar observations*. Icarus, **218**, 771-787.

Feng J.Q., Su Y., Liu J.J., Zheng L., Tan X., Dai S., Li J.-D. and Xing S.-G.; 2013: *Data processing and result analysis of CE-2 MRM*. Earth Sci. (J. China Univ. Geosci.), **38**, 898-906.

Fung A.K., Bredow J. and Tjuatja A.; 2006: *Emission from lunar regolith*. Technical Report.

Hagermann A. and Tanaka S.; 2006: *Ejecta deposit thickness, heat flow, and a critical ambiguity on the Moon*. Geophys. Res. Lett., **33**, 277-305.

Hartmann W.K., Phillips R.J. and Taylor G.J.; 1986: *Origin of the Moon*. The Lunar and Planetary Institute, Houston, 784 pp., ISBN 0-942862-03-1.

Haskin L.A.; 1998: *The Imbrium impact event and the thorium distribution at the lunar highlands surface*. J. Geophys. Res., **103**, 1679-1689.

Hayne P.O., Bandfield J.L., Siegler M.A., Vasavada A.R., Ghent R.R., Williams J.-P., Greenhagen B.T., Aharonson O., Elder C.M., Lucey P.G. and Paige D.A.; 2017: *Global regolith thermophysical properties of the Moon from the diviner lunar radiometer experiment*. J. Geophys. Res. - Planets, **122**, 2371-2400.

Heiken G.H., Vaniman D.T. and French B.M. (eds); 1991: *Lunar sourcebook: a user's guide to the Moon*. NASA, Cambridge University Press, Cambridge, England, 753 pp.

Hiesinger H., Head III J.W., Wolf U., Jaumann R. and Neukum G.; 2010: *Ages and stratigraphy of lunar mare basalts in Mare Frigoris and other nearside maria based on crater size-frequency distribution measurements*. J. Geophys. Res., **115**, E03003, doi: 10.1029/2009JE003380.

Horai K. and Fujii N.; 1972: *Thermophysical properties of lunar material returned by Apollo missions*. The Moon, **4**, 447-475.

Jin Y.Q.; 1998: *Remote sensing theory of electromagnetic scattering and thermal emission*. Science Press, 1998, pp. 118-180.

Jones W.P., Watkins J.R. and Calvert T.A.; 1975: *Temperatures and thermophysical properties of the lunar outmost layer*. The Moon, **13**, 475-494.

Keihm S.J., Peters K. and Langseth M.G.; 1973: *Apollo 15 measurement of lunar surface brightness temperatures*

thermal conductivity of the upper 1 and 1/2 metres of regolith. Earth and Planetary Science Letters, **19**, 337-351.

Korotev R.L.; 1998: *Concentrations of radioactive elements in lunar materials*. Journal of Geophysical Research: Planets (1991-2012), **103(E1)**, 1691-1701.

Lan A.L. and Zhang S.W.; 2004: *Study on the thickness of lunar soil with microwave radiometer*. Remote Sens. Technol. Appl., **19**, 154-158, in Chinese.

Langseth M.G., Keihm S.J. and Peters K.; 1976: *Revised lunar-heat flow values*. In: Proc. 7th Lunar and Planetary Science Conference, Houston, TX, USA, pp. 3143-3171.

Lawrence D.J., Feldman W.C., Barraclough B.L., Binder A.B., Elphic R.C., Maurice S. and Thomsen D.R.; 1998: *Global elemental maps of the Moon: the lunar prospector gamma-ray spectrometer*. Sci., **281**, 1484-1489, doi: 10.1126/science.281.5382.1484.

Lawrence D.J., Feldman W.C., Elphic R.C., Little R.C., Prettyman T.H., Maurice S., Lucey P.G. and Binder A.B.; 2002: *Iron abundances on the lunar surface as measured by the lunar prospector gamma-ray and neutron spectrometers*. J. Geophys. Res. - Planets, **107**, 5130, doi: 10.1029/2001JE001530.

Li Y., Wang Z.Z. and Jiang J.S.; 2010: *Simulations on the influence of lunar surface temperature profiles on CE-1 lunar microwave sounder brightness temperature*. Sci. Chin. Earth Sci., **53**, 1379-1391.

Meng Z.G.; 2008: *Lunar regolith parameters retrieval using radiative transfer simulation and look-up technique*. Ph.D. dissertation, Jilin University, Changchun, China, in Chinese.

Mitchell D.L. and de Pater I.D.; 1994: *Microwave imaging of Mercury's thermal emission at wavelengths from 0.3 to 20.5 cm*. Icarus, **110**, 2-32.

Njoku E. and Kong J.A.; 1977: *Theory for passive microwave remote sensing of near-surface soil moisture*. Journal of Geophysical Research, **82(20)**, 3108-3118.

Olhoeft G.R. and Strangway D.W.; 1975: *Dielectric properties of the first 100 metres of the Moon*. Earth Planet. Sci. Lett., **24**, 394-404.

Paige D.A., Foote M.C., Greenhagen B.T., Schofield J.T., Calcutt S., Vasavada A.R., Preston D.J., Taylor F.W., Allen C.C., Snook K.J., Jakosky B.M., Murray B.C., Soderblom L.A., Jau B., Loring S., Bulharowski J., Bowles N.E., Thomas I.R., Sullivan M.T., Avis C., De Jong E.M., Hartford W. and McCleese D.J.; 2010: *The lunar reconnaissance orbiter diviner lunar radiometer experiment*. Space Sci. Rev., **150**, 125-160.

Rodgers C.D.; 2000: *Inverse methods for atmospheric sounding: theory and practice*. Series on Atmospheric, Oceanic and Planetary Physics, vol. 2, 256 pp., doi: 10.1142/3171.

Spencer J.R., Lebofskyf L.A. and Sykes M.V.; 1989: *Systematic biases in radiometric diameter determinations*. Icarus, **78**, 337-354.

Tsang L., Njoku E. and Kong J.A.; 1975: *Microwave thermal emission from a stratified medium with non uniform temperature distribution*. J. Appl. Phys., **46**, 5127-5133.

Ulaby F.T., Moore R.K. and Fung A.K.; 1981: *Microwave remote sensing: active and passive*. Addison-Wesley Publishing Company, Norwood, MA, USA, 2162 pp.

Urquhart M.L. and Jacksky B.M.; 1997: *Lunar thermal emission and remote determination of surface properties*. J. Geophys. Res., **102**, 10959-10969.

Vasavada A.R., Paige D.A. and Wood S.E.; 1999: *Near-surface temperatures on Mercury and the Moon and the stability of polar ice deposits*. Icarus, **141**, 179-193.

Wang Z.Z., Li Y., Jiang J.S. and Zhang X.; 2008: *Microwave transfer models and brightness temperature simulations of MWS for remote sensing lunar surface on CE-1 satellite*. In: Proc. International Conference on Microwave and Millimeter Wave Technology, Nanjing, China, pp. 1683-1686.

Wang Z.Z., Li Y., Zhang X.H., Shan J.J., Xu C.D., Zhang D.H. and Zhang W.G.; 2010: *Calibration and brightness temperature algorithm of CE-1 lunar microwave sounder (CELMS)*. Sci. China Earth Sci., **53**, 1392-1406, doi: 10.1007/s11430-010-4008-x.

Warren P.H. and Rasmussen K.L.; 1987: *Megaregolith insulation, internal temperatures, and bulk uranium content of the Moon*. J. Geophys. Res.- Solid Earth, **92**, 3453-3465.

Whitaker E.A.; 1981: *The lunar Procellarum basin*. Lunar Planet. Sci., **12A**, 105-111.

Wieczorek M.A. and Phillips R.J.; 2000: *The "Procellarum KREEP Terrane": implications for mare volcanism and lunar evolution*. J. Geophys. Res., **105**, 20417-20430.

Zhang W.J., Zhang X.J. and Li F.; 2008: *Backscattering from multilayer soil and its application to deep soil moisture estimation*. J. Electron. & Inf. Technol., **30**, 2107-2110.

Zhang D.H., Zhang X.H., Wang Z.Z. and Dong X.L.; 2009: *Mechanism of lunar soil depth sounding and ground validation experiment for the CE-1 lunar microwave sounder*. Sci. China Series D-Earth Sci., **39**, 1097-1104.

Corresponding author: Weijia Zhang
Department of AOP Physics, University of Oxford
Parks road, OX1 3PU, Oxford, U.K.
Phone: +44 0741 4878175; e-mail: zhangw@physics.ox.ac.uk